NIR-triggered on-site NO/ROS/RNS nanoreactor: Cascade-amplified photodynamic/photothermal therapy with local and systemic immune responses activation

Ziqing Xu, Yakun Kang, Jie Zhang, Jiajia Tang, Hanyao Sun, Yang Li, Doudou He, Xuan Sha, Yuxia Tang, Ziyi Fu, Feiyun Wu and Shouju Wang

---

Related articles

Large-field objective lens for multi-wavelength microscopy at mesoscale and submicron resolution
Xin Xu, Qin Luo, Jixiang Wang, Yahui Song, Hong Ye, Xin Zhang, Yi He, Minxuan Sun, Ruobing Zhang, Guohua Shi
Opto-Electronic Advances   2024 **7**, 230212   doi: 10.29026/oea.2024.230212

Microchip imaging cytometer: making healthcare available, accessible, and affordable
Xilong Yuan, Todd Darcie, Ziyin Wei, J Stewart Aitchison
Opto-Electronic Advances   2022 **5**, 210130   doi: 10.29026/oea.2022.210130

Terahertz technology in intraoperative neurodiagnostics: A review
Nikita V. Chernomyrdin, Guzel R. Musina, Pavel V. Nikitin, Irina N. Dolganova, Anna S. Kucheryavenko, Anna I. Alekseeva, Yuye Wang, Degang Xu, Qiwu Shi, Valery V. Tuchin, Kirill I. Zaytsev
Opto-Electronic Advances   2023 **6**, 220071   doi: 10.29026/oea.2023.220071

More related article in Opto-Electronic Journals Group website

NIR-triggered on-site NO/ROS/RNS nanoreactor: Cascade-amplified photodynamic/photothermal therapy with local and systemic immune responses activation

Ziqing Xu[1†], Yakun Kang[2†], Jie Zhang[1†], Jiajia Tang[1], Hanyao Sun[1], Yang Li[1], Doudou He[1], Xuan Sha[1], Yuxia Tang[1], Ziyi Fu[3]*, Feiyun Wu[1]* and Shouju Wang[1]*

Photothermal and photodynamic therapies (PTT/PDT) hold promise for localized tumor treatment, yet their full potential is hampered by limitations such as the hypoxic tumor microenvironment and inadequate systemic immune activation. Addressing these challenges, we present a novel near-infrared (NIR)-triggered RNS nanoreactor (PBNO-Ce6) to amplify the photodynamic and photothermal therapy efficacy against triple-negative breast cancer (TNBC). The designed PBNO-Ce6 combines sodium nitroprusside-doped Prussian Blue nanoparticles with Chlorin e6 to enable on-site RNS production through NIR-induced concurrent NO release and ROS generation. This not only enhances tumor cell eradication but also potentiates local and systemic antitumor immune responses, protecting mice from tumor rechallenge. Our *in vivo* evaluations revealed that treatment with PBNO-Ce6 leads to a remarkable 2.7-fold increase in cytotoxic T lymphocytes and a 62% decrease in regulatory T cells in comparison to the control PB-Ce6 (Prussian Blue nanoparticles loaded with Chlorin e6), marking a substantial improvement over traditional PTT/PDT. As such, the PBNO-Ce6 nanoreactor represents a transformative approach for improving outcomes in TNBC and potentially other malignancies affected by similar barriers.

Keywords: photothermal therapy; photodynamic therapy; nitric oxide; reactive nitrogen species; triple-negative breast cancer; immune response; nanoreactor

Introduction

Photothermal and photodynamic therapy (PTT/PDT) activated by a single-wavelength laser presents a promising, safe, and effective approach for treating localized tumors such as breast cancer[1−5]. Our previous work has revealed the synergistic potential of combining PTT and PDT[6,7]. However, the localized nature of phototherapy imposes limitations on its efficacy. While phototherapy

---

[1]Laboratory of Molecular Imaging, Department of Radiology, The First Affiliated Hospital of Nanjing Medical University, Nanjing 210029, China; [2]Department of Breast Surgery, The First Affiliated Hospital of Nanjing Medical University, Nanjing 210029, China; [3]Department of Women & Children Research Center, The First Affiliated Hospital, Nanjing Medical University, Nanjing 210029, China.

†These authors contributed equally to this work.

*Correspondence: ZY Fu, E-mail: ziyi.fu@njmu.edu.cn; FY Wu, E-mail: wfy_njmu@163.com; SJ Wang, E-mail: shouju.wang@gmail.com

can provoke anti-tumor immune responses, it is understood that these localized immunostimulatory effects are insufficient to produce robust systemic anti-tumor immunity[8–10]. Additionally, the hypoxic tumor microenvironment hampers PDT's effectiveness[11,12]. Further research is needed to enhance phototherapy's ability to stimulate systemic anti-tumor immunity and overcome the constraints of the tumor microenvironment.

Nitric oxide (NO) is a unique bioactive molecule with diverse functions in many physiological and pathological processes[13,14]. A key interaction occurs between NO and the reactive oxygen species (ROS) generated by PDT, resulting in the formation of reactive nitrogen species (RNS)[15,16]. These RNS can enhance PDT's efficacy under hypoxic conditions by aiding tumor cell eradication, while also significantly influencing immune responses. Current research indicates the peroxynitrite anion ($ONOO^-$), a type of RNS, can suppress immunosuppressive cells and repolarize tumor-associated macrophages to an M1-like phenotype[17,18]. However, the integration of RNS with PTT/PDT remains scarcely explored, leaving the impacts of the NO/ROS/RNS combination on local and systemic anti-tumor immunity largely unknown.

A considerable hurdle in amplifying PTT/PDT with RNS lies in the precise control of NO release in terms of timing and location[19–21]. Given the short lifetime of singlet oxygen produced during PDT (typically 3–6 ms) and its limited diffusion within cells (approximately 20 nm), positioning NO donors near photosensitizers is imperative to efficiently generate RNS[22]. Traditional approaches injecting NO donors and photosensitizers as separate entities may compromise efficacy due to differing pharmacokinetics[23]. Therefore, we propose unifying photosensitizers and NO donors within single nanoparticles, then utilizing laser irradiation to concurrently initiate PTT/PDT and trigger NO release. This could substantially enhance RNS production and anti-tumor efficacy.

For our study, triple negative breast cancer (TNBC) was chosen as the model system. As the leading malignancy among women worldwide, TNBC exhibits a markedly immunosuppressive and hypoxic tumor environment[24,25]. This milieu impedes therapeutic interventions by suppressing immune cell activity and forming hypoxic regions resistant to PDT[26,27]. Therefore, utilizing the TNBC model is fitting to evaluate the efficacy of RNS generation in conquering these intrinsic tumor microenvironmental challenges. Demonstrating the benefits of this method in TNBC can pave the way for its adoption in tackling other tumors plagued by similar obstacles.

In our work, we developed sodium nitroprusside-doped Prussian Blue nanoparticles (PBNO) as NO nanogenerators and combined them with the photosensitizer Chlorin e6, forming PBNO-Ce6. Under near-infrared (NIR) laser exposure, PBNO-Ce6 underwent a temperature surge, initiating photothermal tumor destruction and catalyzing NO release through cleavage of the Fe-NO bond. Concurrently, the co-loaded Ce6 produced singlet oxygen, transforming NO into RNS that further enhanced PDT/PTT. Our comprehensive evaluation of PBNO-Ce6's therapeutic efficacy in orthotopic and recurrent breast cancer models revealed the NIR-triggered NO/ROS/RNS generation augmented treatment outcomes for primary and secondary tumors, eliciting potent local and systemic immune responses (Scheme 1).

Experimental section/methods

Materials

SNP ($Na_2[Fe(CN)_5NO]\cdot2H_2O$), potassium ferricyanide ($K_3[Fe(CN)_6]$), and polyvinylpyrrolidone (PVP, K29-32) were purchased from Aladdin Industry Corporation (Shanghai, China). Anhydrous ethanol was purchased from Sinopharm Chemical Reagent Co. Ltd. (Shanghai, China). Griess Reagent kit was purchased from Cayman Chemical (Michigan, USA). 3-Amino, 4-aminomethyl-2', 7'-difluorescein, diacetate (DAF-FM DA), 2', 7'-dichlorofluorescein diacetate (DCFH-DA) and 4',6-diamidino-2-phenylindole (DAPI) were obtained from Beyotime Biotechnology (Shanghai, China). The fluorescent probes BBoxiProbe® O56 and BBoxiProbe® O52 were purchased from Bestbio (Beijing, China). 3-(4,5-dimethylthiazol-2-yl)-2,5-diphenyl tetrazolium bromide (MTT, 99.0%) was purchased from Nanjing Keygen Biotech. Co., Ltd. (Nanjing, China). RPMI-1640 medium, phosphate buffer solution (PBS), heat-inactivated fetal bovine serum (FBS), trypsin, and penicillin-streptomycin solution were purchased from Gibco Laboratories (NY, USA). The 4T1 cell line was obtained from the Chinese Academy of Sciences (Shanghai, China). Fixable Viability Dye Fluorescent Dye (FVD) purchased from Thermo Fisher Scientific (MA, USA). Anti-CD45-BV510, anti-CD3-FITC, anti-CD4-BV421, anti-CD8-PerCP-cy5.5, anti-IFN-γ-PE-Cy7, anti-Foxp3-PE and anti-CD25-APC were all from BD Biosciences (New Jersey, USA).
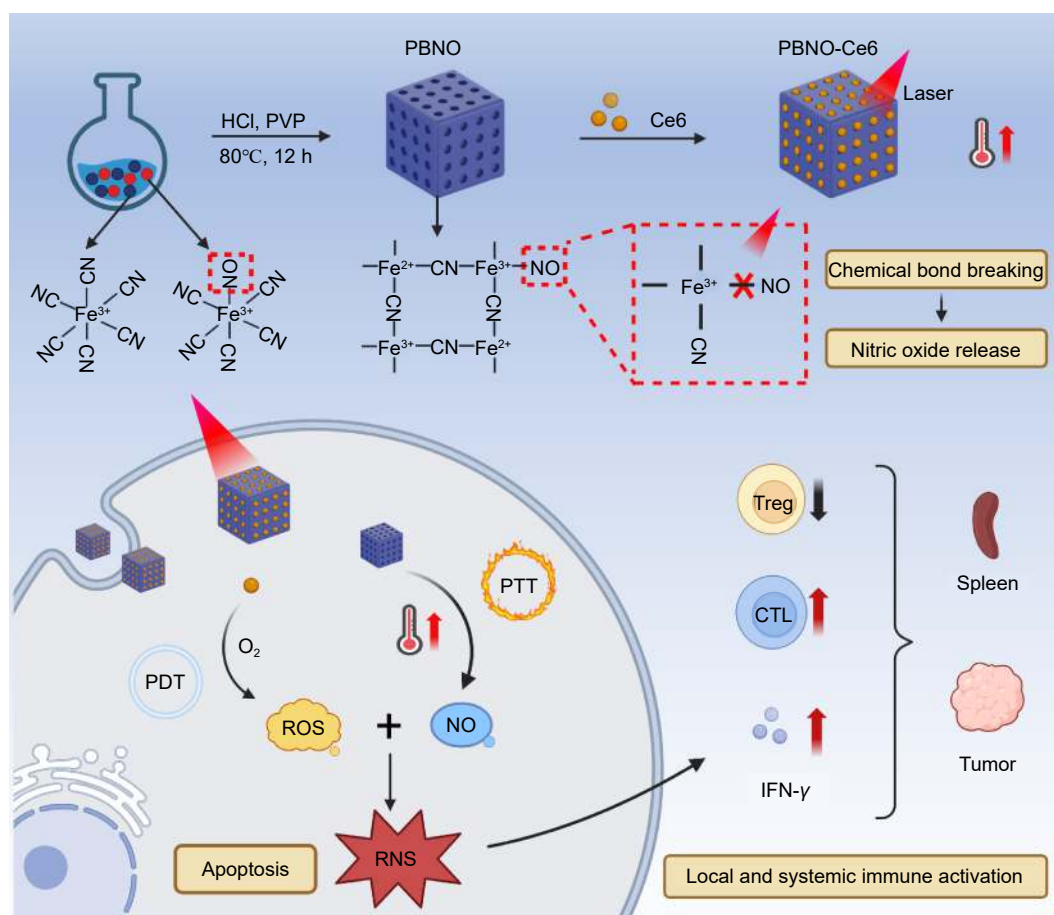
Scheme 1 | Illustration showing the preparation and use of the RNS nanoreactor. The PBNO-Ce6 nanoparticles heat up (PTT) and release NO when exposed to NIR laser. At the same time, ROS are generated (PDT) and further transform the NO into RNS. The combined effect of PTT and RNS-enhanced PDT causes cell apoptosis and promotes strong activation of local and systemic immune responses.

Bioinformatics analysis for identification of the hypoxia environment of breast cancer

To identify the hypoxic environment in breast cancer, immunohistochemistry staining of HIF1A, VEGFA, and GLUT1 in normal breast tissues and breast cancer samples were acquired from The Human Protein Atlas (THPA) database and compared. The expression of HIF1A, VEGFA, and GLUT1 was compared between breast cancer and paired para-cancerous normal breast tissues from 113 patients using data from The Cancer Genome Atlas (TCGA) database[28]. To compare the level of hypoxia between TNBC and non-TNBC patients, the expression of HIF1A, VEGFA and GLUT1 was compared between TNBC (578 patients) and non-TNBC (87 patients) using bc-GenExMiner v5.0[29].

Bioinformatics analysis for identification of the immunosuppressive environment of breast cancer

To identify differences in the immune microenvironment between normal breast tissue and breast cancer,

RNA sequencing data from 1099 breast tumor samples and 292 normal breast tissue samples were obtained from The Cancer Genome Atlas (TCGA) and Genotype-Tissue Expression (GTEx) projects, respectively. A total of 28 immune cell type specific gene sets were curated from Molecular Signatures Database and related publications[30,31]. Gene Set Variation Analysis (GSVA) was performed to estimate the enrichment of each immune cell type specific gene set in each sample.

To estimate the influence of the immune microenvironment on survival, immune scores were calculated for breast cancer samples from TCGA using the estimate R package. OS curves were generated for patients with high immune scores (n=109) and low immune scores (n=938).

To estimate the influence of the immune microenvironment on recurrence risk in breast cancer, processed gene expression and clinical data from 200 patients were obtained from the GEO database (GSE11121). Immune scores were calculated as described above, and DMFS

curves were generated for patients with high immune scores (n=52) and low immune scores (n=148).

To compare the immune microenvironment between TNBC and non-TNBC samples, the single-cell RNA sequencing dataset GSE161529 was obtained from the GEO database. The dataset contained 8 TNBC samples and 8 non-TNBC samples. The sequencing data were filtered, normalized, and scaled prior to linear dimensional reduction with principal component analysis (PCA). The FindNeighbors and FindClusters functions were utilized to cluster cells based on the PCA results, with a resolution of 0.4. Differentially expressed genes were used to annotate the identity of the cell clusters. Further hierarchical clustering was performed on the T cell subgroup using FindSubCluster to achieve higher resolution T cell types. The T cell clusters were annotated based on known T cell markers.

To compare the survival and recurrence risk between TNBC and non-TNBC patients, OS and PFS curves were generated according to the phenotype and clinical data of breast cancer patients from TCGA (661 patients for OS and 586 patients for PFS).

Preparation of PB and PBNO

For the synthesis of PB, 120 mg of potassium ferricyanide and 3 g of PVP were dissolved in 40 mL of HCl (0.01 mol/L) and heated in a 100 mL flask in a water bath at 80 °C for 1 h. The synthesized PB was collected by centrifugation (14000 rpm for 8 min) and washed at least 3 times with water. To synthesize PBNO, 488.7 mg SNP, 60 mg potassium ferricyanide, and 3 g PVP were dissolved in 40 mL HCl (0.1 mol/L), mixed in a 100 mL flask, and heated in a water bath at 80 °C for 12 h. The synthesized PBNO was collected by centrifugation (14000 rpm for 8 min) and washed at least 3 times with water[32].

Preparation of PBNO-Ce6

To prepare PBNO-Ce6, 5 mg of Ce6 was dissolved in 5 mL of H_2O, mixed with 5 mL of PBNO (2 mg·mL^{-1}) dispersed in H_2O, shaken at 500 rpm in a metal bath at room temperature for 24 h and centrifuged at 13500 rpm for 8 min to collect the nanoparticles.

To investigate the loading capacity and efficacy of PBNO-Ce6, 1 mL of PBNO (1 mg·mL^{-1}) was mixed with 1 mL of different concentrations of Ce6 solution and shaken for 24 h at room temperature. The mixture was centrifuged and the Ce6 concentration in the supernatant

was calculated from the standard curve of Ce6 (Fig. S15). The Ce6 loading capacity and loading efficacy of PBNO-Ce6 were calculated according to the following formulas:

Loading Capacity of Ce6 (%) = [weight of loaded Ce6 / (weight of PBNO-Ce6 + weight of loaded Ce6)] × 100%,

Loading Efficiency of Ce6 (%) = [weight of loaded Ce6 / weight of totally Ce6] × 100%.

Characterization

Transmission electron microscopy (TEM) of the nanoparticles was conducted using a FEI Talos F200X electron microscope operating at 200 kV. The zeta potential and hydrodynamic sizes (DLS) were measured with a Brookhaven analyser (Brookhaven Instruments Co., Holtsville, USA). Nitrogen sorption analysis was performed on a Micromeritics Tristar 3000 at –196 °C. The Brunauer-Emmett-Teller (BET) method was used to determine the specific surface area based on adsorption data at p/p_0 = 0.05–0.15. The total pore volume was determined from adsorption data at p/p_0 = 0.995. UV–vis spectra were obtained using a UV-vis-near infrared (NIR) spectrophotometer (UV-3600, Shimadzu). Fluorescence intensity measurements were performed using a fluorescence spectrophotometer at specific excitation wavelengths (F97, Shanghai Lengguang Technology Co., Ltd). Fluorescent images were taken with an inverted fluorescent microscope (Axio Vert.A1, Zeiss). Flow cytometry analyses were conducted using a Beckman Cytoflex flow cytometer (Cytoflex, Beckman).

Photothermal properties of PB and PBNO

PB and PBNO solutions with concentrations between 0 to 0.2 mg·mL^{-1} were irradiated by a 660-nm laser at power densities from 0.2 to 0.8 W·cm^{-2} for 10 minutes. The temperature change was monitored by an IR camera. To assess the photothermal stability of the nanoparticles, the PBNO solution was irradiated with a 660 nm laser for 10 minutes, the laser was turned off and the solution was allowed to return to room temperature, then this cycle was repeated 5 times. The photothermal conversion efficacy (η) was determined according to previous reports[33].

NO/ROS/RNS generation detection

To detect the generation of NO, PBNO solutions at specified concentrations were irradiated by a 660-nm laser at different power densities for 30 minutes with or without an ice bath. Then the solutions were centrifuged and the NO concentration in the supernatant was determined by

standard curve of NO (Fig. S16) using Griess reagent kit following the manufacturer's instructions.

To detect the generation of ROS, 50 µg mL^{-1} concentration PB and equal concentration PBNO, PB-Ce6 and PBNO-Ce6 solutions were irradiated by a 660-nm laser at 0.4 W·cm^{-2} for 5 minutes. The generation of singlet oxygen was detected by SOSG following the manufacturer's instructions.

To detect the generation of RNS, PBNO-Ce6 solutions were irradiated by a 660-nm laser at 0.4 W·cm^{-2}. PBNO and PB-Ce6 solutions with equal light irradiation dosage and PBNO-Ce6 with no irradiation served as controls. The generated RNS was determined by the fluorescent probe BBoxiProbe® O56 following the manufacturer's instructions.

In vitro NO/ROS/RNS generation detection

4T1 cells were seeded at a density of 8×10^4 cells well^{-1} in 24-well plates and incubated with 100 µg mL^{-1} PBNO-Ce6 and corresponding concentrations of Ce6, PBNO, and PB-Ce6 for 4 hours. The cells were then irradiated with a 660 nm laser at 0.4 W·cm^{-2} for 5 minutes. The generation of NO, ROS and RNS was detected by Griess reagent, DAF-FM DA and BBoxiProbe® O52 respectively, following the manufacturer's instructions for each reagent.

In vitro cytotoxicity

To assess the biocompatibility of PBNO-Ce6, 4T1 cells were seeded in 96-well plates at a density of 8 × 10^3 cells well^{-1} and incubated at 37 °C 5% CO$_2$ for 24 hours. The cells were then incubated overnight with different concentrations of PB, PBNO or PBNO-Ce6. Cell viability was measured by MTT assay.

To assess the therapeutic efficacy of PBNO-Ce6, the cells were incubated with different concentrations of PB, PBNO and PBNO-Ce6 for 4 hours, then irradiated with a 660 nm laser at 0.4 W·cm^{-2} for 5 minutes. Cells treated with PBNO-Ce6 and irradiated with the laser while incubated in an ice bath served as a control to nullify photothermal therapy effects. The cells were stained with Calcein AM and PI following the manufacturer's instructions and imaged by fluorescence microscopy. The synergy between PDT and PTT effect induced by PBNO-Ce6 upon laser irradiation was evaluated by determining the combination index (CI) using the Chou-Talalay method[34]. CI values are then calculated using the following formula:

$$CI = \frac{D_{PDT/PTT}}{D_{PTT}} + \frac{D_{PDT/PTT}}{D_{PDT}} , \qquad (1)$$

where D_{PTT} is the IC50 of PBNO + laser, D_{PDT} is the IC50 of PBNO-Ce6 + laser (with ice bath), $D_{PDT/PTT}$ is the IC50 of PBNO-Ce6 + laser.

Cell apoptosis assay

4T1 cells were seeded at a density of 8×10^5 cells per well in 6-well plates and cultured for 24 hours. The cells were then treated with PB, PBNO, PB-Ce6 and PBNO-Ce6 for 12 hours, followed by irradiation with a 660 nm laser at 0.4 W·cm^{-2} for 5 minutes. After an additional 8 hours, the cells were collected and stained with Annexin V-FITC and propidium iodide (PI), then analyzed by flow cytometry.

Animal tumor mode

Female BALB/c mice (6 weeks old) were subcutaneously injected on the flank with a suspension of 1×10^5 4T1 breast cancer tumor cells in 100 µL PBS. The tumors were allowed to grow until reaching a volume of approximately 100 mm^3 before being used for experiments. All animal experiments were performed in compliance with the guidelines for the care and use of laboratory animals, ethical approval for this studywas obtained from Animal Ethics Committee of Nanjing Medical University (2202006).

In vivo distribution

Tumor-bearing mice were intravenously injected with 100 µL of PBNO-Ce6 (10 mg·mL^{-1}) or an equivalent amount of free Ce6. *In vivo* fluorescence imaging was performed at 0, 1, 2, 4, 8, 12 and 24 hours post-injection to observe fluorescence intensity at the tumor site. Additionally, 20 µL blood samples were collected from the tail vein at 10, 15, 30, 60, 120, 240 and 480 minutes post-injection. The fluorescence intensity at 660 nm was measured for the blood samples.

In vivo antitumor efficacy

30 tumor-bearing mice were randomly divided into 5 treatment groups (*n*=6 per group): (I) Saline + laser; (II) Ce6 + Laser; (III) PBNO + Laser; (IV) PB-Ce6 + Laser; (V) PBNO-Ce6 + Laser. Mice were injected with saline, PBNO-Ce6 (15 mg·mL^{-1}) or an equivalent amount of Ce6, PBNO, or PB-Ce6. The tumors were then irradiated with a 660-nm laser at a power density of 0.4 W·cm^{-2} for 15 minutes. 24 hours post-treatment, one mouse per

group was euthanized and the tumors collected for H&E and TUNEL staining. The generation of NO, ROS and RNS in tumors was detected by Griess reagent, DAF-FM DA and BBoxiProbe® O52 respectively, following the manufacturer's instructions for each reagent.

The weights of the remaining mice and tumor growth were recorded every other day for 14 days post-treatment. Tumor volume was calculated using the formula: $width^2 \times length/2$.

An additional 30 mice were grouped and treated as described above to monitor survival time over a prolonged period.

Immunophenotyping

Seven days after treatment, tumors and spleens were collected from mice in each treatment group. The tissues were mechanically dissociated into single cell suspensions in PBS, then enzymatically digested with 5 mg·mL^{-1} collagenase IV at 37 °C for 1.5 hours with shaking. The cell suspensions were passed through a 70 μm cell strainer, incubated in RBC lysis buffer, and resuspended in RPMI 1640 medium with 10% FBS.

The isolated immune cells were stimulated by adding phorbol 12-myristate 13-acetate (PMA) and incubating for 4 hours at 37 °C with shaking. The cells were then stained with fluorescently-labeled antibodies against FVD, CD45, CD3, CD4, CD8a, and CD25 for 30 minutes at 4 °C in the dark. To evaluate cytotoxic T cell efficacy and proliferation, cells were also stained with antibodies against Foxp3, IFN-γ, and Ki67. The stained cell suspensions were analyzed by flow cytometry on a Beckman Coulter CytoFLEX. The gating strategy was shown in Fig. S17.

Tumor rechallenging

12 mice were divided into three groups (*n*=4 per group): Saline + Laser, PBNO + Laser, and PBNO-Ce6 + Laser, and treated as previously described. Seven days after the initial treatment, 1×10^5 4T1 cells were injected into the opposite flank of each mouse to establish secondary tumors. The growth curves of the secondary tumors were then monitored over time.

Biocompatibility study *in vivo*

Six female healthy BALB/c mice (6 weeks old, 20 g ± 2 g) were divided into two groups (*n*=3 per group) and intravenously injected with either 100 μL saline or 100 μL of PBNO-Ce6 (10 mg·mL^{-1}). After one week, blood samples were collected for biochemical and blood cell counts. Major organs including hearts, livers, spleens, lungs and kidneys were collected and sectioned for H&E staining to assess toxicity.

Statistical analysis

Data are presented as means ± standard deviation of ≥3 independent experiments performed. Student t-test was used for comparison between two groups. Statistical significance (*p*) was displayed as *p< 0.05, **p< 0.01, ***p< 0.001, ****p< 0.0001.

Results and discussion

Identification of hypoxia and immune suppressive environment in human TNBC

To evaluate the hypoxic state in human triple-negative breast cancer (TNBC), we selected three proteins, HIF1A, VEGFA, and GLUT1, as biomarkers of tumor hypoxia. HIF1A becomes stabilized and activated under low oxygen conditions, characterizing tumor hypoxia[35]. The expression of VEGFA, driven by HIF1A, induces angiogenesis, thereby catering to the increased oxygen and nutrient demands of hypoxic tumors[36]. Meanwhile, GLUT1, encoding a glucose transporter protein, facilitates the augmented glucose uptake by cancer cells under hypoxia as a metabolic countermeasure[37].

Utilizing immunohistochemistry staining, we discerned pronounced positive staining for HIF1A, VEGFA, and GLUT1 in human breast cancer tissues, contrasting with the subdued staining observed in their normal counterparts (Fig. 1(a)). A subsequent analysis of the TCGA database echoed our findings, registering a marked surge in the expression levels of HIF1A, VEGFA, and GLUT1 when juxtaposed against normal breast tissue (Figs. 1(b)&S1). Intriguingly, the expression of these biomarkers was more accentuated in TNBC samples compared to non-TNBC malignancies (Fig. 1(c)). Collectively, these findings attest to the ubiquity of hypoxia in the human TNBC microenvironment.

The tumor microenvironment (TME) is a dynamic entity, with its immunological constituents playing a pivotal role in determining the risk of cancer recurrence. Bioinformatics analysis revealed a more immunosuppressive milieu in human breast cancer tissues, characterized by decreased anti-tumor immune infiltrates, such as mast cells and eosinophil cells, and a concomitant escalation in pro-tumor immune cell constituents, notably regulatory T cells and myeloid-derived suppressor cells (Fig. S2). In line with this, survival analysis of breast
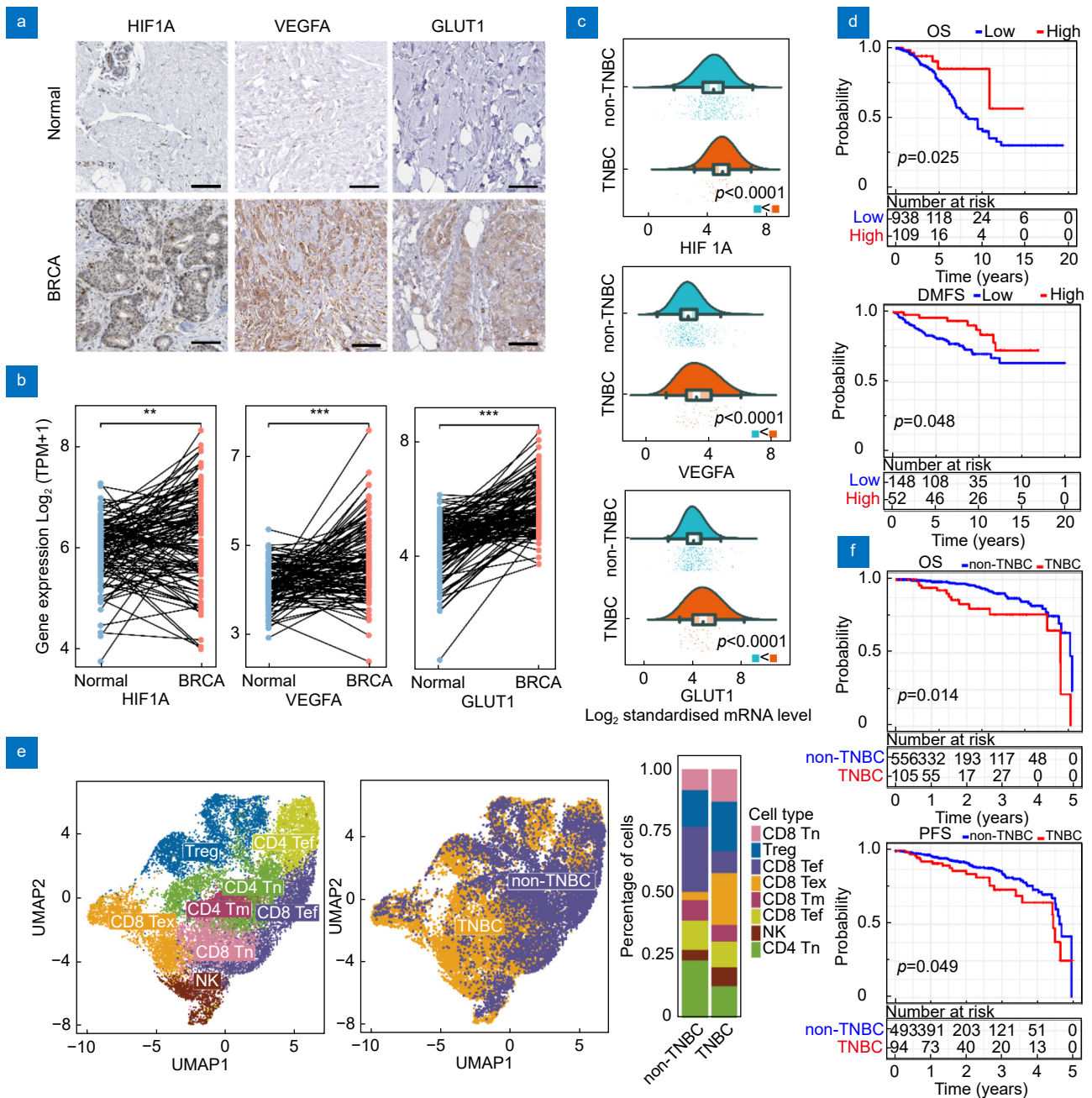
Fig. 1 | Bioinformatics analysis of breast cancer patients. (**a**) Immunohistochemistry images showing HIF1A, VEGFA, and GLUT1 staining in breast cancer tumor tissue and normal breast tissue. Scale bar: 100 μm. (**b**) HIF1A, VEGFA, and GLUT1 gene expression profiles across TCGA/GTEx breast cancer datasets. (**c**) Differential expression of HIF1A, VEGFA, and GLUT1 in TNBC compared to non-TNBC. (**d**) Kaplan-Meier survival curves for OS and DMFS in patients with high vs low immune scores. (**e**) Single cell analysis of T cells in TNBC and non-TNBC tumors. (Tn: naive T cells; Tef: effector T cells; Tex: exhausted T cells; Tm: memory T cells; Tef: effector memory T Cell.) (**f**) Kaplan-Meier survival curves for OS and PFS in TNBC and non-TNBC patients.

cancer patients (Fig. 1(d)) showed that patients with lower immune scores, indicating lower anti-tumor immune infiltrates, had significantly shorter overall survival (OS) and distant metastasis-free survival (DMFS). These findings underscore the profound prognostic implications of the intratumoral immune landscape in human breast cancer.

To explore the immune intricacies of human breast cancer, we analyzed single-cell sequencing data from 8 TNBC and 8 non-TNBC human breast cancer tissue samples (Figs. 1(e)&S3). Astoundingly, TNBC samples manifested an overwhelming prevalence of immunosuppressive cell populations, encompassing Treg cells and exhausted CD8 T cells, juxtaposed with a paucity of

anti-tumor cell populations, like effector CD8 T cells and CD4 T cells. Consequently, survival analysis indicated that TNBC patients experienced notably reduced OS and progression-free survival (PFS) compared to non-TNBC patients (Fig. 1(f)). The aforementioned findings indicate that human TNBC possesses an immunosuppressive microenvironment, predisposing it to relapse and metastasis. Consequently, the development of therapeutic strategies aimed at immune activation emerges as imperative.

Preparation and characterization of PBNO-Ce6

We embedded the nitric oxide donor, sodium nitroprusside (SNP), into Prussian Blue nanoparticles (PB) due to its structural similarity to the PB precursor, potassium ferricyanide. To integrate nitric oxide with Prussian blue nanoparticles (PB), we embedded the nitric oxide donor, sodium nitroprusside (SNP), utilizing its structural congruence to potassium ferricyanide, the precursor for PB synthesis. Transmission electron microscopy (TEM) displayed PBNO nanoparticles as cubic structures with an average size of 108.7 ± 3.3 nm (Fig. 2(a)). Fourier-transform infrared (FT-IR) spectra exhibited pronounced stretching vibrations for the CN group at 2086 cm^{-1} and the N=O group at 1944 cm^{-1}, indicative of successful SNP incorporation (Fig. 2(b))[38]. N$_2$ adsorption-desorption isotherms confirmed that PBNO retained PB's consistent mesopores, with a modified BJH pore diameter at 4.1 nm (Fig. 2(c)). The PBNO had a Brunauer-Emmett-Teller (BET) surface area of 473.0 m^2·g^{-1} and a mesopore volume of 0.073 cm^3·g^{-1}.

Taking advantage of its mesoporous structure, PBNO allowed for efficient photosensitizer incorporation. UV-vis spectra determined a Ce6 loading capacity for PBNO-Ce6 up to 94.5%, with an efficiency exceeding 64.4% (Fig. 2(d)). Post Ce6 incorporation, the nanoparticle's hydrodynamic diameter augmented from 197.5 ± 3.8 nm to 215.7 ± 5.3 nm, and the zeta potential shifted from -21.7 ± 3.7 mV to -32.5 ± 1.6 mV (Fig. 2(e)). The PBNO-Ce6 showed similar fluorescence spectrum with free Ce6 (Fig. S4). The UV-vis spectra of PBNO-Ce6 presented distinct Ce6 peaks around both 400 nm and 650 nm, validating the Ce6's successful integration with PBNO (Fig. 2(f)).

The photothermal capabilities of both PB and PBNO were assessed by gauging temperature variations in their solutions upon near-infrared (NIR) laser exposure. Both solutions displayed temperature augmentations influ-

enced by power density and concentration (Figs. 2(g)&S5). Post a 10-minute exposure to a low-power density laser (0.4 W·cm^{-2}), the PB solution's temperature reached 50.1 °C, while PBNO peaked at 41.2 °C. In contrast, pure water remained virtually unaltered (Fig. 2(h)). PBNO showed commendable photothermal stability through five heat-cooling cycles (Fig. S6). Derived heat-cooling curves deduced a photothermal conversion rate of 61.2% for PBNO, marginally less than PB's 79.2% (Figs. 2(i)&S7). This discrepancy can likely be attributed to the energy consumed in breaking the Fe-NO bonds.

NO/ROS/RNS generation ability of PBNO-Ce6

To understand the multifaceted reactive species production capabilities of PBNO-Ce6 (Fig. 3(a)), we began by assessing its nitric oxide (NO) generation through Griess assay. Figure 3(b) illustrates that PBNO's NO production escalated with increased irradiation power density and extended exposure time, underscoring that NIR laser-induced photothermal actions facilitate NO release. PBNO, when incubated in an ice bath, showed no NO production.

Singlet oxygen, a type of ROS, can oxidize NO to form RNS. SOSG assays revealed that PBNO-Ce6 and PB-Ce6 generated comparable amounts of singlet oxygen under NIR exposure (Fig. 3(c)), suggesting that SNP incorporation didn't impair PB-Ce6's ability to produce singlet oxygen. Neither PBNO nor PB produced singlet oxygen, solidifying the idea that Ce6 was responsible for its generation.

RNS production was gauged by assessing ONOO$^-$ generation through the BBoxiProbe® O56 probe. Figure 3(d) displays that only post-NIR exposure did PBNO-Ce6 produce RNS. Neither PB-Ce6 nor PBNO exhibited such an effect, inferring that simultaneous NO emission and singlet oxygen formation in the proximity of PBNO-Ce6 lead to RNS. RNS production by PBNO-Ce6 was directly related to laser intensity, as shown in Figs. 3(e)&S8.

In vitro outcomes mirrored these findings (Figs. 3(f)&3(h)). Both fluorescence imaging and flow cytometry attested to NO production in cells exposed to PBNO and PBNO-Ce6 post-NIR illumination. ROS was discerned in cells with Ce6, PB-Ce6, and PBNO-Ce6 treatment. RNS detection was exclusive to PBNO-Ce6-treated cells, with its presence coinciding with ROS. This reinforces that the co-generation of NO and ROS around PBNO-Ce6, activated by NIR exposure, is pivotal for RNS formation.
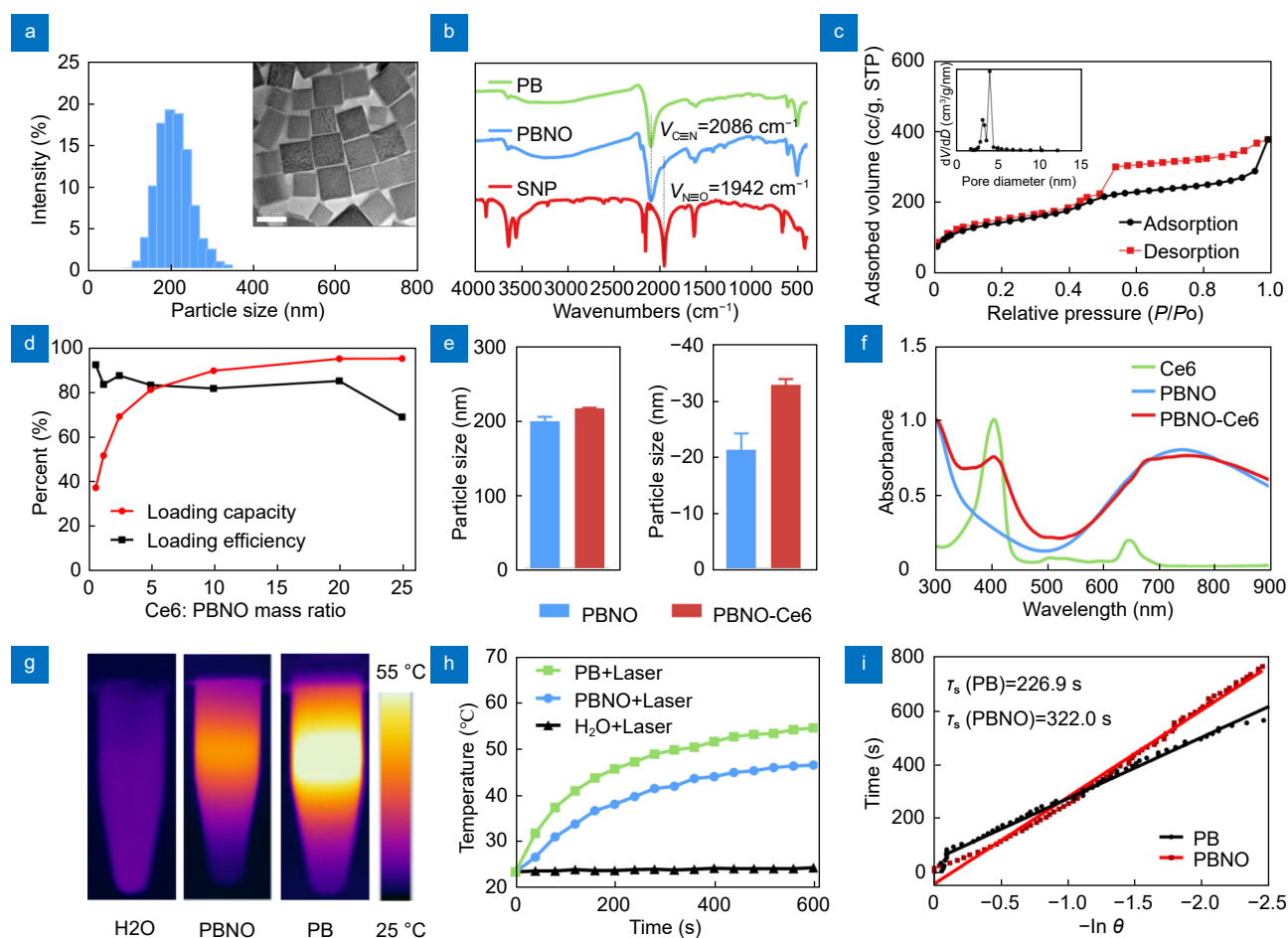
Fig. 2 | Characterization of PBNO-Ce6 nanoparticles. (**a**) Particle size distribution and TEM image of PBNO. (**b**) FT-IR spectra of PB, PBNO and SNP. (**c**) N_2 adsorption-desorption isotherms of PBNO. (**d**) Loading capacity and efficiency of Ce6 on PBNO. (**e**) Size and zeta potential of PBNO and PBNO-Ce6. (**f**) UV-vis absorption spectra of PBNO, Ce6 and PBNO-Ce6. (**g**) Thermographs of H_2O, PB and PBNO irradiated by 660-nm laser under 0.4 W cm^{-2}. (**h**) Corresponding photothermal heating curves of H_2O, PB and PBNO. (**i**) Linear time vs -lnθ plots obtained from the cooling period of PB and PBNO.

In vitro cytotoxicity

The promising potential of PB nanoparticles for therapeutic applications largely stems from their excellent biocompatibility. Validating this, MTT assays demonstrated that the addition of SNP and Ce6 to form PBNO and PBNO-Ce6 did not compromise this inherent biocompatibility, as negligible cytotoxicity was observed in the absence of laser irradiation (Fig. 4(a)).

Yet, the therapeutic potential of PBNO-Ce6 truly shone upon laser irradiation. The cytotoxicity levels of 4T1 breast cancer cells for PBNO-Ce6 were noticeably higher compared to its counterpart, PB-Ce6, at equivalent concentrations. This suggests that RNS generation by PBNO-Ce6 has the capability to amplify PDT/PTT outcomes, even if PBNO possesses somewhat diminished photothermal toxicity relative to the native PB (Fig. 4(b)).

The therapeutic efficacy of PBNO-Ce6, endowed with both photothermal (PTT) and photodynamic (PDT) properties, was further evaluated against controls. Compared to cells treated with PB, which manifests only PDT effects, and cells subjected to an ice bath during PBNO treatment, effectively nullifying its PTT effects, the cells treated with PBNO-Ce6 showed a pronounced reduction in viability (Fig. 4(c)). To explore whether the enhanced efficacy of PBNO-Ce6 was merely an additive outcome of its dual modalities or a result of a synergistic interaction, we calculated its combination index. The notably low value of 0.24 confirmed a synergistic effect between its PDT and PTT properties (Fig. S9).

To further elucidate the heightened efficacy of PBNO-Ce6, live/dead staining was conducted. The results demonstrated a pronounced red fluorescence for PBNO-Ce6, indicative of extensive cell death, in stark contrast
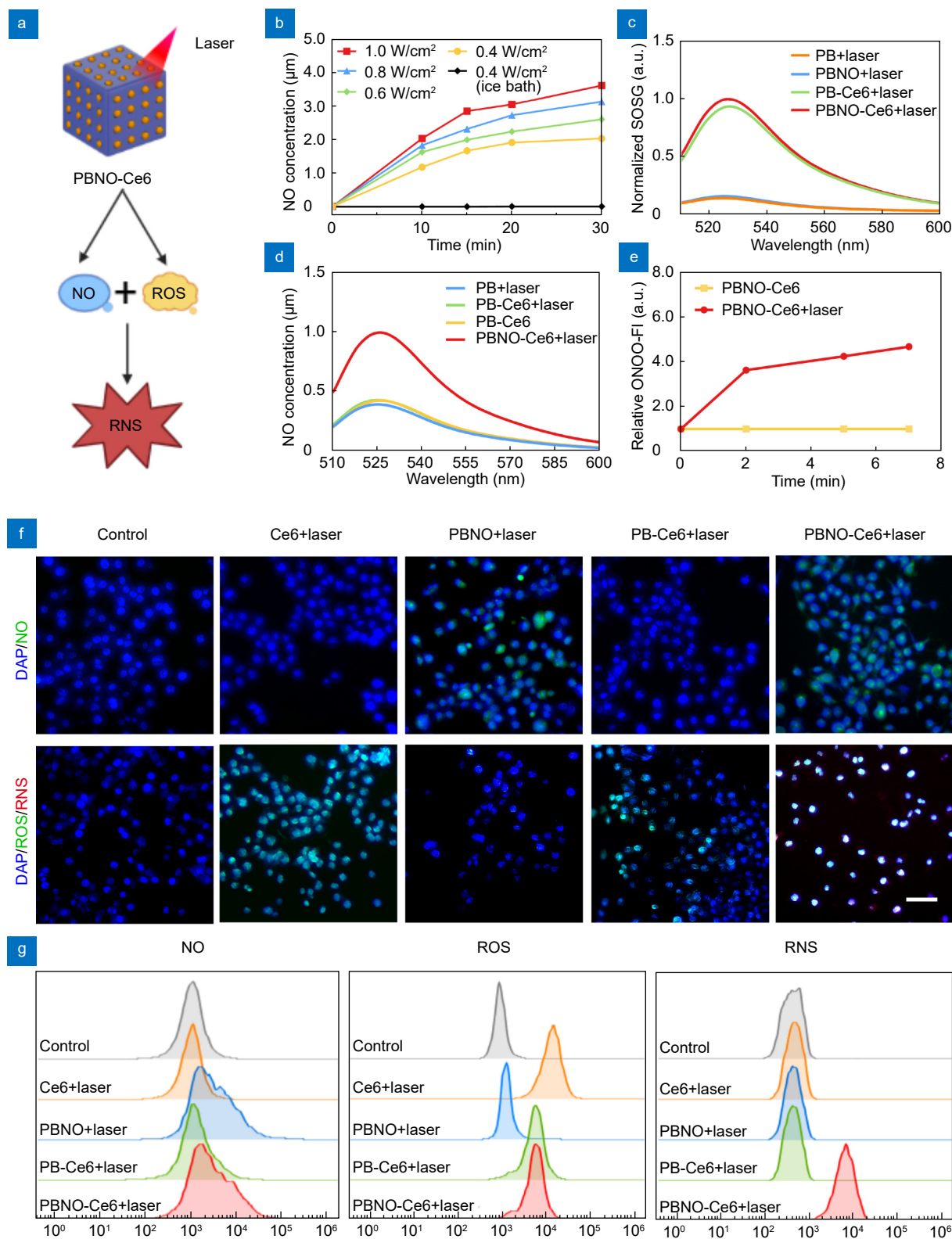
Fig. 3 | NIR triggered generation of NO/ROS/RNS by PBNO-Ce6. (**a**) Scheme showing NO/ROS/RNS generation. (**b**) NO release detected after laser irradiation of PBNO. (**c**) ROS generation detected by SOSG fluorescence of PB, PBNO, PB-Ce6, and PBNO-Ce6 after laser irradiation. (**d**) RNS generation detected by BBoxiProbe® O56 fluorescence of PB, PBNO, PB-Ce6, and PBNO-Ce6 after laser irradiation. (**e**) BBoxiProbe® O56 fluorescence intensity over time. (**f**) Fluorescence images of 4T1 cells stained with probes for NO (DAM-FM DA), ROS (DCFH-DA) and RNS (BBoxiProbe® O52). Scale bar: 50 μm. (**g**) Corresponding flow cytometry analysis of 4T1 cells stained with DAM-FM DA, DCFH-DA and BBoxiProbe® O52.
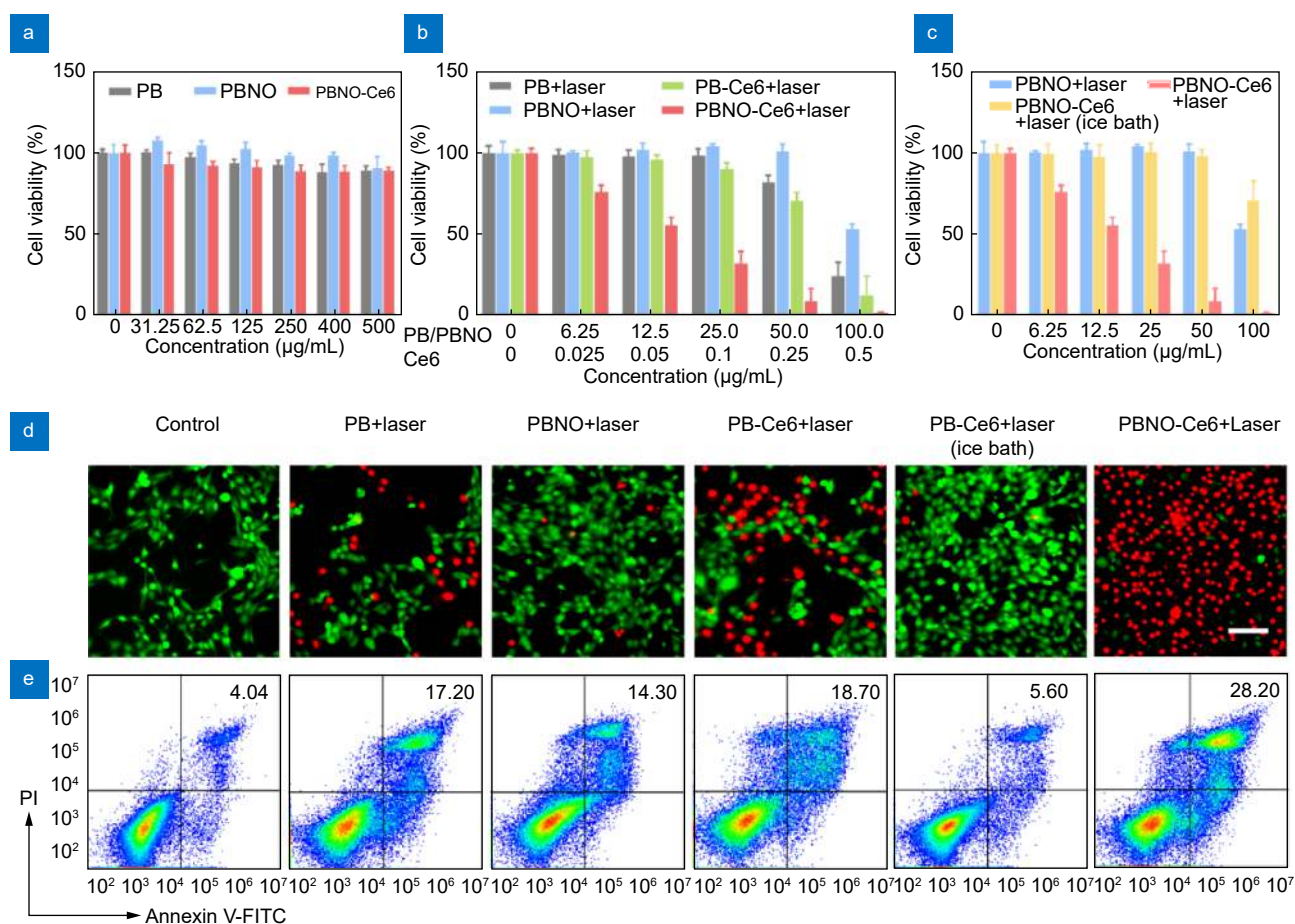
Fig. 4 | *In vitro* therapeutic efficacy of PBNO-Ce6. (**a**) Viability of 4T1 cells after 24 h incubation with PB, PBNO and PBNO-Ce6 without laser irradiation. (**b**) Viability of 4T1 cells after 24 h incubation with PB, PBNO, PB-Ce6 or PBNO-Ce6 and irradiated at 660 nm (0.4 W·cm^{-2}, 5 min). (**c**) Viability of 4T1 cells incubated with PBNO and PBNO-Ce6 (with or without ice bath cooling) for 24 h and irradiated at 660 nm. (**d**) Fluorescence imaging of Calcein-AM and PI stained 4T1 cells after different treatments (concentration: 50 μg·mL^{-1}). Green: Calcein-AM; Red: PI. Scale bar: 50 μm. (**e**) Flow cytometry analysis of apoptosis in 4T1 cells after different treatments (concentration: 25 μg·mL^{-1}).

to the more prevalent green fluorescence observed for other nanoparticles (Fig. 4(d)). Importantly, flow cytometry analysis, as detailed in Fig. 4(e), revealed that cells treated with PBNO-Ce6 underwent the most pronounced transition from viable to late apoptotic/dead states. This was evidenced by a 1.5-fold increase in apoptotic indices compared to PB-Ce6, underscoring the superior apoptosis-inducing capability of PBNO-Ce6.

In vivo distribution and therapeutic efficacy of PBNO-Ce6

The *in vivo* biodistribution of PBNO-Ce6 was assessed in 4T1 tumor-bearing mice. Mice were intravenously injected with either Ce6 or PBNO-Ce6, and the accumulation of PBNO-Ce6 in tumors was monitored. A peak in tumor-associated fluorescence was observed at 8 h post-injection, indicative of maximum PBNO-Ce6 accumulation (Figs. 5(a)&S10). Moreover, the systemic circula-

tion half-life of PBNO-Ce6 was found to be 2.3 times longer than that of free Ce6. This superior retention and tumor targeting is attributed to the extended blood circulation of PBNO-Ce6 in comparison to free Ce6 (Fig. S11).

For therapeutic efficacy assessment, 4T1 tumor-bearing mice were grouped and administered with equal dosages of Ce6, PBNO, PB-Ce6, PBNO-Ce6, or PBS as a reference, followed by NIR laser irradiation. Notably, the temperatures of tumors treated with PBNO, PB-Ce6, and PBNO-Ce6 reached 50 °C upon irradiation, showcasing the comparable photothermal capabilities of PBNO-Ce6 to PBNO and PB-Ce6 *in vivo* (Figs. 5(b)&5(c)&S12). Analysis of fluorescently stained tumor sections post-irradiation confirmed exclusive NO, ROS, and RNS generation in the PBNO-Ce6 group (Fig. 5(d)). This observation is consistent with previous *in vitro* findings and further underscores NIR-induced NO/ROS/RNS production
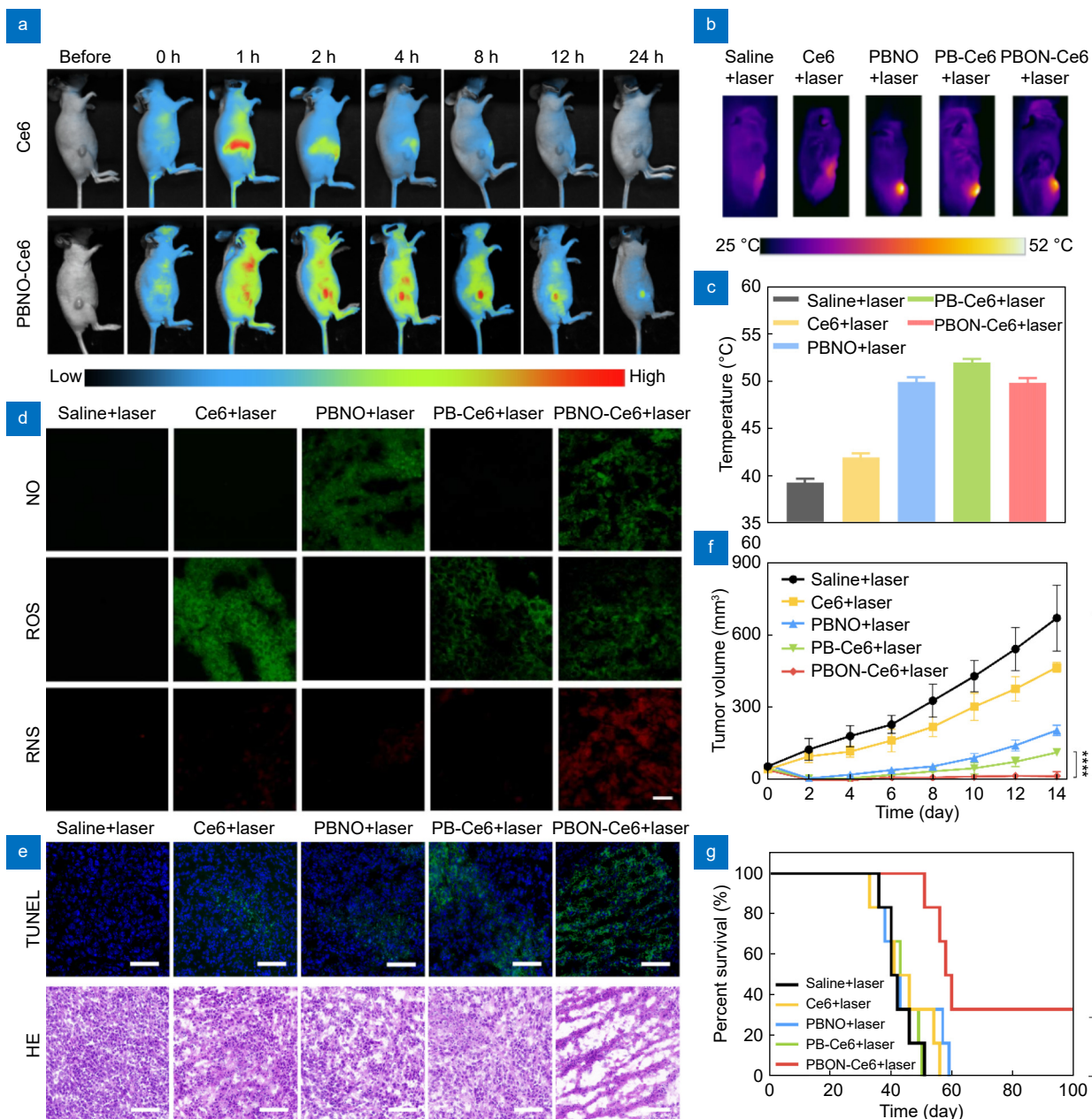
Fig. 5 | *In vivo* therapeutic efficacy of PBNO-Ce6. (**a**) Fluorescence images of mice at different time points after intravenous injection of free Ce6 or PBNO-Ce6. (**b**) Thermal images of mice during laser irradiation. (**c**) Temperature changes at the tumor area after irradiation. (**d**) Fluorescence imaging of NO, ROS and RNS generation in tumors. (**e**) TUNEL and H&E staining of tumors after treatment. Scale bar: 50 μm. (**f**) Tumor growth curves of mice after different treatments. (**g**) Kaplan-Meier survival curves of mice in different treatment groups. (*$p< 0.05$, **$p< 0.01$,***$p< 0.001$, ****$p< 0.0001$)

by PBNO-Ce6. Additionally, TUNEL and H&E stained sections highlighted pronounced apoptosis and necrosis in tumors treated with PBNO-Ce6, underscoring the potent antitumor activity mediated by RNS (Fig. 5(e)). After 14 days of monitoring, tumors treated with PBNO-Ce6 exhibited significantly reduced volumes compared to those treated with PB-Ce6 (Fig. 5(f)). Furthermore, PBNO-Ce6 treatment led to a marked improvement in survival durations relative to other nanoparticle treat-

ments (Fig. 5(g)). In sum, these findings validate the augmented antitumor efficacy of PBNO-Ce6 in primary breast cancer, attributed to the NIR triggered NO/ROS/RNS generation.

Antitumor immune response

Breast cancer recurrence and metastasis following primary treatments remain significant challenges in oncology. To evaluate the potential of combined PBNO-Ce6

and NIR laser irradiation in preventing long-term recurrence, post-treatment mice were subsequently rechallenged with 4T1 breast cancer cells. Mice subjected to the combined PBNO-Ce6 and NIR laser treatment exhibited significant resistance to the tumor rechallenge compared to those treated with native or PBNO alone (Figs. 6(a)&S13). This resistance suggests a potent antitumor immune response activated by the NO/ROS/RNS generation facilitated by the combined PBNO-Ce6 and NIR laser irradiation.

Delving deeper into the immune responses engendered by this combined treatment, immunophenotyping was performed on isolated primary tumors and spleens. Flow cytometry analyses revealed that the combined treatment led to a marked increase in intratumoral CD3+CD8+ cytotoxic T cells (CTLs) and a notable decrease in immunosuppressive CD25+Foxp3+ regulatory T cells (Tregs) compared to other treatments (Fig. 6(b)). Notably, CTLs increased 2.7-fold while Tregs decreased

62% in the PBNO-Ce6 group compared to the PB-Ce6 group, indicating the potent ability of RNS generated by PBNO-Ce6 to stimulate antitumor immunity and inhibit immunosuppression. Similar trends were observed in the spleen (Fig. 6(c)), signifying that the combination of PBNO-Ce6 and NIR laser therapy influences both the tumor microenvironment and systemic lymphoid organs by promoting CTLs and suppressing Tregs.

In addition to these shifts in CTL and Treg populations, the efficacy and proliferative capability of CTLs post-treatment were assessed. Elevated frequencies of both IFN-gamma-producing and Ki-67-marked proliferating CD8+ T cells were found in tumors and spleens of the combined treated mice, underscoring its profound effect (Fig. 6(d)&6(e)). In summary, these findings highlight the capability of the combined PBNO-Ce6 and NIR laser irradiation to enhance both systemic and localized antitumor immune reactions, offering substantial protection against breast cancer recurrence.
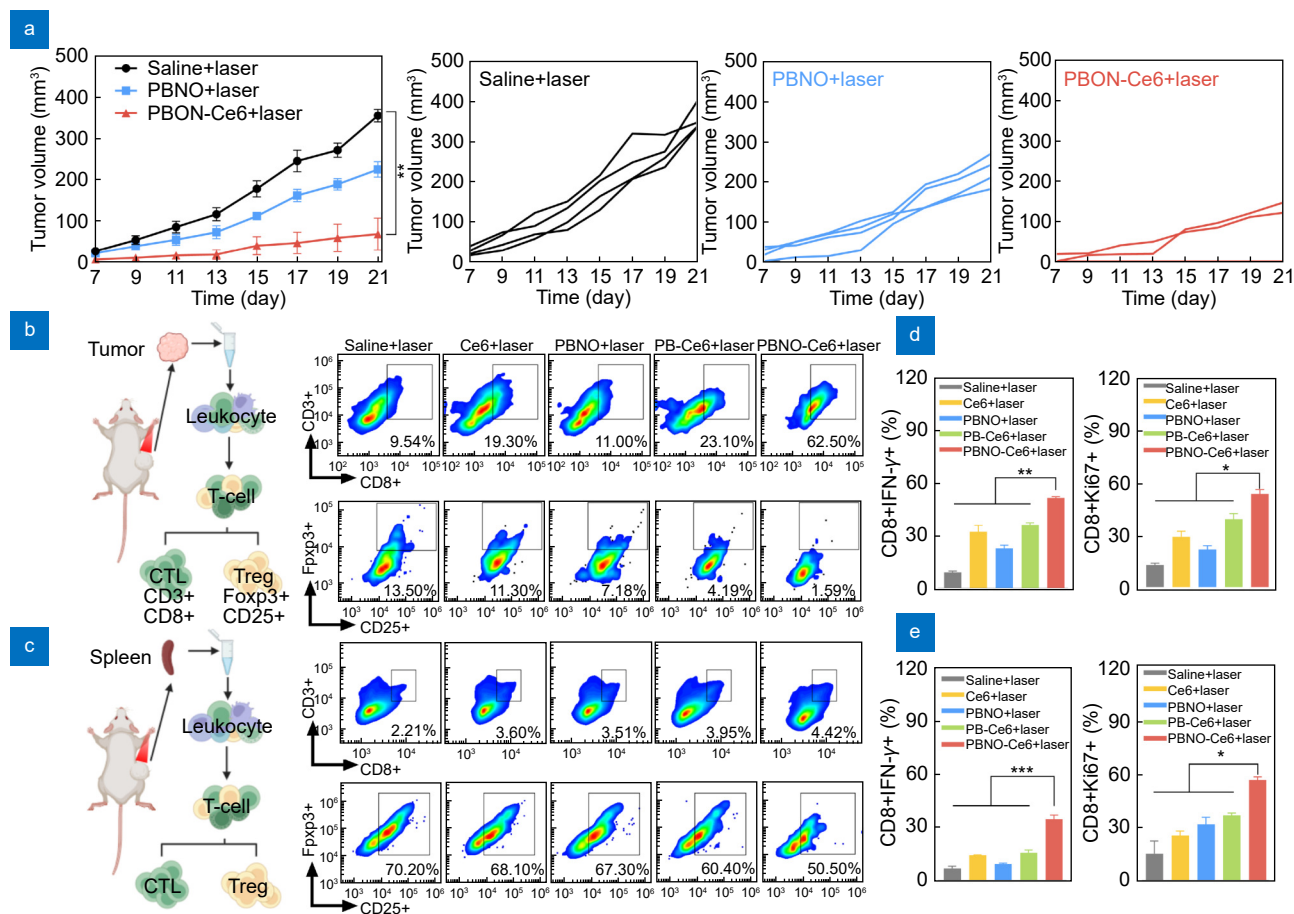

Fig. 6 | Local and systemic antitumor immune responses induced by PBNO-Ce6 treatment. (a) Tumor growth curves of mice after tumors rechallenge in different treatment groups. (b, c) Flow cytometry analysis of immunosuppressive Tregs (CD4+Foxp3+CD25+) and antitumor CTLs (CD3+CD8+) in (b) primary tumors and (c) spleens. (d, e) Analysis of IFN-γ+ and Ki67+ expression in CTLs in (d) primary tumors and (e) spleens. (*$p < 0.05$, **$p < 0.01$,***$p < 0.001$, ****$p < 0.0001$)

Biocompatibility *in vivo*

The *in vivo* biocompatibility of PBNO-Ce6 was systematically assessed. Mice were administered either PBNO-Ce6 or saline and observed for a span of 14 days. During this period, no significant deviations in body weight were observed following PBNO-Ce6 administration (Fig. S14). Histological examinations using H&E staining of major organ tissues revealed no noticeable pathological changes or indications of damage (Fig. 7(a)). A comprehensive range of hematological indicators, such as white blood and red blood cell counts (Fig. 7(b)), as well as various biochemical markers like alanine transaminase and aspartate aminotransferase (Fig. 7(c)), were analyzed. These parameters consistently fell within conventional limits for both PBNO-Ce6 and saline-injected mice, indicating no discernible differences between the two groups.

These findings collectively suggest that PBNO-Ce6 does not induce any apparent adverse effects within the 14-day observation window, highlighting its promising biocompatibility profile.

Conclusions

In summary, we have developed a NIR-triggered RNS nanoreactor (PBNO-Ce6) to combat TNBC, which exhibits a highly immunosuppressive and hypoxic tumor microenvironment. PBNO-Ce6 comprises sodium nitroprusside-doped Prussian Blue nanoparticles and the photosensitizer Chlorin e6. By harnessing concurrent production of NO and ROS, PBNO-Ce6 can efficiently generate RNS, which greatly enhanced the photodynamic/photothermal therapeutic efficacy against TNBC. Furthermore, the RNS potently stimulated localized and
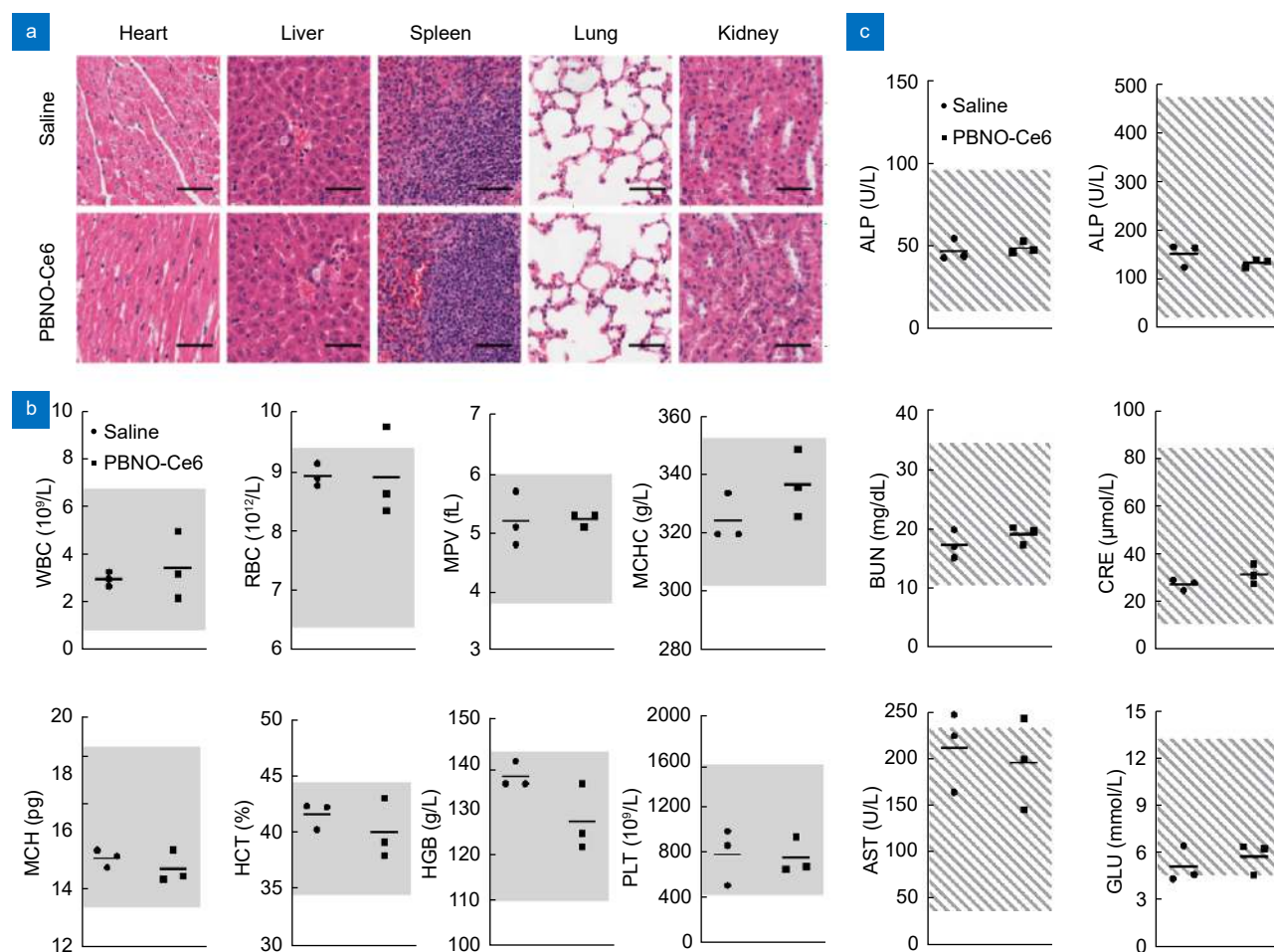

Fig. 7 | Biocompatibility of PBNO-Ce6 *in vivo*. (**a**) H&E images of heart, liver, spleen, lung, and kidney tissues from mice at 14 days post-injection. Scale bar: 50 μm. (**b**) Routine blood cell count of mice at 14 days post-injection. WBC: white blood cells; RBC: red blood cells; MPV: mean platelet volume; MCHC: mean corpuscular hemoglobin concentration; MCH: mean corpuscular hemoglobin; HCT: hematocrit; HGB: hemoglobin; PLT: platelet count. The gray areas indicate the normal range of the indicators. (**c**) Blood biochemistry analysis of mice at 14 days post-injection. ALT: alanine aminotransferase; ALP: alkaline phosphatase; BUN: blood urea nitrogen; CRE: creatinine; AST: aspartate aminotransferase; GLU: glucose.

systemic antitumor immune responses, protecting mice from tumor rechallenge. This resulted in a 2.7-fold increase in cytotoxic T lymphocytes and a 62% decrease in regulatory T cells compared to PB-Ce6. To our knowledge, PBNO-Ce6 is the first NIR-triggered RNS nanoreactor with synergistic photodynamic/photothermal effects and robust immune-stimulating activity. Our design strategy could serve as a versatile platform to incorporate with immune checkpoint inhibitors or chemotherapies, further improving outcomes for TNBC and other malignancies.

References

1. Overchuk M, Weersink RA, Wilson BC et al. Photodynamic and photothermal therapies: synergy opportunities for nanomedicine. *ACS Nano* **17**, 7979–8003 (2023).
2. Shen S, Qiu JC, Huo D et al. Nanomaterial-enabled photothermal heating and its use for cancer therapy via localized hyperthermia. *Small* **20**, 2305426 (2024).
3. Yang HY, Liu RF, Xu YX et al. Photosensitizer nanoparticles boost photodynamic therapy for pancreatic cancer treatment. *Nanomicro Lett* **13**, 35 (2021).
4. Hu TT, Wang ZD, Shen WC et al. Recent advances in innovative strategies for enhanced cancer photodynamic therapy. *Theranostics* **11**, 3278–3300 (2021).
5. Lee D, Kwon S, Jang SY et al. Overcoming the obstacles of current photodynamic therapy in tumors using nanoparticles. *Bioact Mater* **8**, 20–34 (2022).
6. Yuan C, Li Y, Xu ZQ et al. Imaging-guided synergistic photo-chemotherapy using doxorubicin-loaded gadolinium porphyrin-based metal-organic framework nanosheets. *ACS Appl Nano Mater* **5**, 15318–15327 (2022).
7. Wang SJ, Huang P, Nie LM et al. Single continuous wave laser induced photodynamic/plasmonic photothermal therapy using photosensitizer-functionalized gold nanostars. *Adv Mater* **25**, 3055–3061 (2013).
8. Yang S, Sun B, Liu F et al. NIR-II imaging-guided mitochondrial-targeting organic nanoparticles for multimodal synergistic tumor therapy. *Small* **19**, 2207995 (2023).
9. Yue J, Mei Q, Wang PY et al. Light-triggered multifunctional nanoplatform for efficient cancer photo-immunotherapy. *J Nanobiotechnol* **20**, 181 (2022).
10. Li ZL, Lai XQ, Fu SQ et al. Immunogenic cell death activates the tumor immune microenvironment to boost the immunotherapy efficiency. *Adv Sci (Weinh)* **9**, 2201734 (2022).
11. Wang MY, He MY, Zhang MY et al. Controllable hypoxia-activated chemotherapy as a dual enhancer for synergistic cancer photodynamic immunotherapy. *Biomaterials* **301**, 122257 (2023).
12. Zhao M, Zhang YY, Miao J et al. An activatable phototheranostic probe for anti-hypoxic type i photodynamic- and immunotherapy of cancer. *Adv Mater* **36**, 2305243 (2024).
13. Yun HY, Dawson VL, Dawson TM. Nitric oxide in health and disease of the nervous system. *Mol Psychiatry* **2**, 300–310 (1997).
14. Marletta MA. Nitric oxide: biosynthesis and biological significance. *Trends Biochem Sci* **14**, 488–492 (1989).
15. Chang MY, Wang M, Liu YH et al. Dendritic plasmonic CuPt alloys for closed-loop multimode cancer therapy with remarkably enhanced efficacy. *Small* **19**, 2206423 (2023).
16. Chen Y, Li ZH, Pan P et al. Tumor-specific ONOO⁻ nanogenerator for improved drug delivery and enhanced chemotherapy of tumor. *ACS Nano* **15**, 11514–11525 (2021).
17. Shi MH, Zhang JL, Wang Y et al. Tumor-specific nitric oxide generator to amplify peroxynitrite based on highly penetrable nanoparticles for metastasis inhibition and enhanced cancer therapy. *Biomaterials* **283**, 121448 (2022).
18. Ji CW, Si JX, Xu Y et al. Mitochondria-targeted and ultrasound-responsive nanoparticles for oxygen and nitric oxide codelivery to reverse immunosuppression and enhance sonodynamic therapy for immune activation. *Theranostics* **11**, 8587–8604 (2021).
19. Beurton J, Boudier A, Barozzi Seabra A et al. Nitric oxide delivering surfaces: an overview of functionalization strategies and efficiency progress. *Adv Healthc Mater* **11**, 2102692 (2022).
20. van der Vlies AJ, Yamane S, Hasegawa U. Recent advance in self-assembled polymeric nanomedicines for gaseous signaling molecule delivery. *Wiley Interdiscip Rev Nanomed Nanobiotechnol* **16**, e1934 (2024).
21. Gao D, Asghar S, Hu RF et al. Recent advances in diverse nanosystems for nitric oxide delivery in cancer therapy. *Acta Pharm Sin B* **13**, 1498–1521 (2023).
22. Tavakkoli Yaraki M, Liu B, Tan YN. Emerging strategies in enhancing singlet oxygen generation of nano-photosensitizers toward advanced phototherapy. *Nanomicro Lett* **14**, 123 (2022).
23. So JY, Ohm J, Lipkowitz S et al. Triple negative breast cancer (TNBC): non-genetic tumor heterogeneity and immune microenvironment: emerging treatment options. *Pharmacol Ther* **237**, 108253 (2022).
24. Jia HY, Truica CI, Wang B et al. Immunotherapy for triple-negative breast cancer: existing challenges and exciting prospects. *Drug Resist Updat* **32**, 1–15 (2017).
25. Chen X, Iliopoulos D, Zhang Q et al. XBP1 promotes triple-negative breast cancer by controlling the HIF1α pathway. *Nature* **508**, 103–107 (2014).
26. Ding MC, Shao K, Wu LJ et al. A NO/ROS/RNS cascaded-releasing nano-platform for gas/PDT/PTT/immunotherapy of tumors. *Biomater Sci* **9**, 5824–5840 (2021).
27. Ma SJ, Zhao Y, Lee WC et al. Hypoxia induces HIF1α-dependent epigenetic vulnerability in triple negative breast cancer to confer immune effector dysfunction and resistance to anti-PD-1 immunotherapy. *Nat Commun* **13**, 4118 (2022).
28. Thomas AA, Fisher JL, Rahme GJ et al. Regulatory T cells are not a strong predictor of survival for patients with glioblastoma. *Neuro Oncol* **17**, 801–809 (2015).
29. Zhang J, Xu ZQ, Li Y et al. Theranostic mesoporous platinum nanoplatform delivers halofuginone to remodel extracellular matrix of breast cancer without systematic toxicity. *Bioeng Transl Med* **8**, e10427 (2023).
30. Gotwals P, Cameron S, Cipolletta D et al. Prospects for combining targeted and conventional cancer therapy with immunotherapy. *Nat Rev Cancer* **17**, 286–301 (2017).
31. Racle J, de Jonge K, Baumgaertner P et al. Simultaneous enumeration of cancer and immune cell types from bulk tumor gene expression data. *eLife* **6**, e26476 (2017).
32. Feng T, Wan JY, Li P et al. A novel NIR-controlled NO release of sodium nitroprusside-doped Prussian blue nanoparticle for synergistic tumor treatment. *Biomaterials* **214**, 119213 (2019).

33. Wang SJ, Ma XQ, Hong XH et al. Adjuvant photothermal therapy inhibits local recurrences after breast-conserving surgery with little skin damage. *ACS Nano* **12**, 662–670 (2018).

34. Tallarida RJ. Quantitative methods for assessing drug synergism. *Genes Cancer* **2**, 1003–1008 (2011).

35. Wu QH, You L, Nepovimova E et al. Hypoxia-inducible factors: master regulators of hypoxic tumor immune escape. *J Hematol Oncol* **15**, 77 (2022).

36. Wei HM, Xu ZM, Chen LC et al. Long non-coding RNA PAARH promotes hepatocellular carcinoma progression and angiogenesis via upregulating HOTTIP and activating HIF-1α/VEGF signaling. *Cell Death Dis* **13**, 102 (2022).

37. Hoskin PJ, Sibtain A, Daley FM et al. GLUT1 and CAIX as intrinsic markers of hypoxia in bladder cancer: relationship with vascularity and proliferation as predictors of outcome of ARCON. *Br J Cancer* **89**, 1290–1297 (2003).

38. Lynch MS, Cheng M, Van Kuiken BE et al. Probing the photoinduced metal-nitrosyl linkage isomerism of sodium nitroprusside in solution using transient infrared spectroscopy. *J Am Chem Soc* **133**, 5255–5262 (2011).

Acknowledgements

Author contributions

All authors commented on the manuscript.

Z. Q. Xu: Conceptualization, Methodology, Writing - Original Draft; Yakun Kang: Methodology, Data Curation; J. Zhang: Visualization, Investigation, Writing - Original Draft; J. J. Tang: Methodology, H. Y. Sun: Software, Validation; Y. Li: Resource; D. D. He: Investigation; X. Sha: Validation; Y. X. Tang: Visualization, Writing - Review & Editing; Z. Y. Fu: Supervision, Funding Acquisition; F. Y. Wu: Supervision, Project administration; S. J. Wang: Conceptualization, Funding Acquisition,Supervision, Writing - Review & Editing

Competing interests

The authors declare no competing financial interests.

Ethical statement

The conduct of all experiments was in strict adherence to the Guidelines for Animal Experimentation of the Animal Experimentation Ethics Committee of Nanjing Medical University.

Supplementary information

Supplementary information for this paper is available at
https://doi.org/10.29026/oea.2024.240013

Scan for Article PDF